Chemical Engineering Journal 446 (2022) 137439

Contents lists available at ScienceDirect

Chemical Engineering Journal

journal homepage: www.elsevier.com/locate/cej

Developing silicalite-1 encapsulated Ni nanoparticles as sintering-/coking-resistant catalysts for dry reforming of methane

Shanshan Xu [a,*], Thomas J.A. Slater [b], Hong Huang [c], Yangtao Zhou [d], Yilai Jiao [d], Christopher M.A. Parlett [a,b,e,f], Shaoliang Guan [g], Sarayute Chansai [a], Shaojun Xu [e,h], Xinrui Wang [a], Christopher Hardacre [a,*], Xiaolei Fan [a]

[a] Department of Chemical Engineering and Analytical Science, School of Engineering, The University of Manchester, Oxford Road, Manchester M13 9PL, United Kingdom
[b] Electron Physical Science Imaging Centre, Diamond Light Source Ltd., Oxfordshire OX11 0DE, United Kingdom
[c] Electrochemical Process Engineering (IEK-14), Forschungszentrum Jülich GmbH, Jülich 52425, Germany
[d] Shenyang National Laboratory for Materials Science, Institute of Metal Research, Chinese Academy of Sciences, 72 Wenhua Road, Shenyang 110016, China
[e] UK. Catalysis Hub, Research Complex at Harwell, Harwell, Rutherford Appleton Laboratory, Oxfordshire OX11 0FA, United Kingdom
[f] University of Manchester at Harwell, Diamond Light Source, Harwell Science and Innovation Campus, Didcot, Oxfordshire OX11 0DE, United Kingdom
[g] Harwell XPS–The EPSRC National Facility for Photoelectron Spectroscopy, Research Complex at Harwell, Didcot OX11 0FA, United Kingdom
[h] Cardiff Catalysis Institute, School of Chemistry, Cardiff University, Cardiff CF10 3AT, United Kingdom

ARTICLE INFO

Keywords:
Silicalite-1
Encapsulated Ni catalyst
Dry reforming of methane
Anti-sintering
Anti-coking

ABSTRACT

The stability of catalysts in dry reforming of methane (DRM) is a known issue. In this paper an encapsulation strategy has been employed to improve the stability compared with conventional impregnation methods. Herein, nickel nanoparticles encapsulated in silicalite-1 were prepared using a range of methods including post treatment, direct hydrothermal and seed-directed methods to investigate the effect of synthesis protocol on the properties of catalysts, such as degree of encapsulation and Ni dispersion, and anti-coking/-sintering performance in DRM. The Ni@SiO_2-S1 catalysts obtained by the seed-directed synthesis presented the full encapsulation of Ni NPs by the zeolite framework with small particle sizes (~2.9 nm) and strong metal-support interaction, which could sterically hinder the migration/aggregation of Ni NPs and carbon deposition. Therefore, Ni@SiO_2-S1 showed stable CO_2/CH_4 conversions of 80% and 73%, respectively, with negligible metal sintering and coking deposition (~0.5 wt%) over 28 h, which outperformed the other catalysts prepared. In contrast, the catalysts developed by the post-treatment and ethylenediamine-protected hydrothermal methods showed the co-existence of Ni phase on the internal and external surfaces, *i.e.* incomplete encapsulation, with large Ni particles, contributing to Ni sintering and coking. The correlation of the synthesis-structure-performance in this study sheds light on the design of coking-/sintering-resistant encapsulated catalysts for DRM.

1. Introduction

Methane (CH_4) and carbon dioxide (CO_2) are two of the main greenhouse gases, which contribute to current environmental issues (*e.g.,* global warming and climate changes) significantly [1]. Hence, the development of an efficient process to activate and convert CH_4 and CO_2 simultaneously into valuable chemicals is a promising and practical solution to achieve the carbon reduction goal [2]. Catalytic dry reforming of methane (DRM) has attracted great interest because it utilises CH_4 and CO_2 for the direct production of syngas (*i.e.,* CO + H_2) with the theoretical H_2/CO molar ratio approximately 1, which is the essential feedstock to produce value-added oxygenated chemicals and long-chain hydrocarbons *via* Fischer-Tropsch reactions [3,4].

Theoretically, DRM (*i.e.,* $CH_4 + CO_2 \rightarrow 2CO + 2H_2$, $\Delta H^{\circ}_{298K} = +247.3$ kJ mol^{-1}) is highly endothermic which requires high temperature (typically > 600 °C), and thus high energy consumption [5]. Nickel based catalysts are commonly used for DRM due to their good catalytic activities and relatively low cost compared to catalysts based on noble metals (such as Pt, Ru and Rh) [6]. However, Ni-based catalysts commonly suffer from catalyst deactivation during DRM, which is caused by (i) metal particle sintering at high reaction temperatures (*e.g.,* 700 °C) and (ii) carbon deposition induced by methane cracking and CO

* Corresponding authors.
E-mail addresses: shanshan.xu@manchester.ac.uk (S. Xu), c.hardacre@manchester.ac.uk (C. Hardacre).

https://doi.org/10.1016/j.cej.2022.137439
Received 20 January 2022; Received in revised form 23 May 2022; Accepted 6 June 2022
Available online 8 June 2022

disproportionation, being the major limitation for the large-scale industrial applications [7,8]. Therefore, the development of novel Ni-based catalysts with resistance to metal sintering and coking is urgently needed for progressing the industrial DRM. Various strategies have been proposed and explored to increase the catalytic activity and stability of Ni-based reforming catalysts, including the methods of (i) reducing the particle sizes [9,10], (ii) using promoters [11,12], (iii) developing bimetallic catalysts [6,13,14], and (iv) encapsulating metal nanoparticles (NPs) to form unique architectures such as core–shell and yolk-shell structures [15,16]. In comparison with metal NPs supported on the external surface of supports, confinement of metal NPs leads to improved metal stability (by preventing sintering) and coking resistance (by suppressing carbon diffusion on the metal particles) [17,18]. For example, core–shell Ni@SiO_2 catalysts with small Ni NPs (~5 nm) showed a good stability of 50 h in DRM, which could be attributed to the confinement of Ni NPs by the silica shell (to avoid sintering) and the small size of Ni NPs (to reduce carbon diffusion in Ni crystals) [19].

Zeolites with uniform micropores, high specific surface area and high thermal stability (especially siliceous zeolites such as silicalite-1) are considered as promising supports to spatially confine metal particles within their frameworks to form metal@zeolite catalysts, being able to prevent the aggregation and deactivation of metallic species [20]. For example, Pt, Pd, Rh and Ag NPs encapsulated within Beta and silicalite-1 zeolites have been demonstrated to be sintering resistant at 600–700 °C and showed long reaction lifetimes in catalytic C1 chemistry including the water–gas shift reaction, oxidative reforming of methane and CO_2 hydrogenation [21]. Although encapsulated catalyst structures have been reported in previous studies, the relevant synthesis methods can strongly affect the physiochemical properties of catalysts, including metal particle sizes, degree of encapsulation and metal-support interactions, thus influencing the catalytic performance during high-temperature catalysis such as DRM [20]. For example, Ni encapsulated in hollow silicalite-1 developed by a post-treatment method could suppress carbon formation during DRM, showing about 10% carbon deposition after 6 h on stream (compared to ~ 30% carbon deposition on the impregnated Ni/silicalite-1 catalyst). However, large Ni NPs were still found on the external surface of the zeolite support, which led to coke formation and a significant decrease of the CO_2/CH_4 conversion (~62%) after a 20 h test in DRM [22]. By comparison, silicalite-1 encapsulated Pt NPs (<2 nm) prepared by a water-in-oil microemulsion successfully achieved the full encapsulation structure, that is, most Pt NPs was encapsulated within the zeolite. However, the collapse of zeolite structure at > 620 °C caused a decreased accessibility of active sites to the reactant, and hence severe deactivation at high reaction temperatures [23]. Hence, systematic insights into the synthesis-structure-performance relationships in the encapsulated metal NPs (within zeolite crystals) catalysts are needed for the rational development of stable and high-performing catalysts for DRM.

Herein, encapsulated Ni NPs within silicalite-1 (S-1) catalysts were prepared by different synthesis methods (including a post treatment method, direct hydrothermal and seed-directed synthesis) and were investigated comparatively in DRM to assess their catalytic performance. The effect of synthesis methods on the properties of catalysts including degree of encapsulation, Ni dispersion, zeolite shell structure and metal-support interactions and the catalytic performance (in DRM) was investigated. The supported Ni on S-1 catalyst prepared by the conventional wet impregnation method was used as the reference catalyst for comparison. The longevity (up to 28 h) of the catalysts under investigation showed that 5Ni@SiO_2-S1 catalyst (with the full encapsulation structure) developed by the seed-directed synthesis method presented the comparatively best stability with insignificant metal sintering and coking during DRM due to the small Ni particle size and complete confinement of Ni in S-1 zeolite promoted by this method.

2. Experimental

2.1. Preparation of catalysts

2.1.1. Chemicals

Tetrapropylammonium hydroxide solution (TPAOH, 40% in H_2O), tetraethyl orthosilicate (TEOS, 98%), ammonium hydroxide solution (28% in H_2O), urea (BioUltra, >99.5%), nickel nitrate hexahydrate (Ni$(NO_3)_2{\cdot}6H_2O$, ≥97%) and ethylenediamine ($NH_2CH_2CH_2NH_2$, ≥99.5%) were purchased from Sigma-Aldrich. All chemicals were used as received.

2.1.2. Synthesis of silicalite-1 (S-1) zeolite

The S-1 zeolite was prepared by a hydrothermal method with a starting molar composition of SiO_2: TPAOH: H_2O (1:0.4:35). Typically, 8.32 g of TEOS, 8.125 g of TPAOH aqueous solution, and 25 g of H_2O were mixed and stirred at room temperature (RT) for 6 h to form a clear solution. Then, the mixture was transferred into a 50 mL Teflon-lined autoclave and was hydrothermally treated at 170 °C for 3 days. Centrifugation was used to separate the solid products from the liquid phase, and the obtained solid product was washed with deionised (DI) water several times, and then dried at 110 °C in the oven overnight. Finally, the obtained sample was calcined in a muffle furnace at 550 °C for 8 h (1 °C min^{-1}) to remove the organic template.

2.1.3. Synthesis of supported Ni catalyst on S-1 catalyst (Ni/S-1) by impregnation

Supported Ni NPs (theoretical loading of 5.0 wt%) on S-1 zeolite was prepared by incipient wetness impregnation. Typically, 2.5 g of the calcined S-1 was suspended in DI water (30 mL), then 0.619 g of Ni$(NO_3)_2{\cdot}6H_2O$ was added to the suspension. After vigorous stirring for 3 h, the precipitate was evaporated at 80 °C under stirring. Finally, the obtained solid was calcined in a muffle furnace at 550 °C for 6 h (1 °C min^{-1}). The resulting sample is denoted as 5Ni/S-1.

2.1.4. Synthesis of hollow S-1 encapsulated Ni catalyst by post treatment (Ni@hol S-1)

Hollow S-1 encapsulated Ni catalyst was prepared by treating 5Ni/S-1 hydrothermally with TPAOH solution. Typically, 1.0 g of 5Ni/S-1 was mixed with 0.2 M TPAOH solution (40 mL) and stirred for 1 h at RT. The mixture was then transferred into a 100 mL Teflon-lined autoclave, and the system was left at 170 °C for 2 days. The obtained product was centrifuged, washed with DI water, and dried at 110 °C in an oven overnight. Finally, the obtained sample, denoted as 5Ni@hol S-1, was calcined in a muffle furnace at 550 °C for 6 h (1 °C min^{-1}).

2.1.5. Direct hydrothermal synthesis of encapsulated Ni in S-1 catalyst (Ni@EDA-S1)

To enable the direct encapsulation of Ni species in the framework of S-1, ethylenediamine coordinated Ni, *i.e.,* [Ni$(NH_2CH_2CH_2NH_2)_3$]$(NO_3)_2$, was used as the precursor and introduced during the hydrothermal synthesis of S-1 zeolite [24]. Specifically, the molar composition was 1SiO_2: 0.4TPAOH: 35H_2O: 0.05 [Ni$(NH_2CH_2CH_2NH_2)_3$]$(NO_3)_2$, and the synthesis condition was same to that for preparing S-1, as described above. [Ni$(NH_2CH_2CH_2NH_2)_3$]$(NO_3)_2$ was prepared by dissolving 0.95 g of Ni$(NO_3)_2{\cdot}6H_2O$ into 2 mL ethylenediamine and 8 mL H_2O mixture under stirring at RT. Then the precursor was added dropwise into the clear solution of TEOS, TPAOH and H_2O under stirring for 30 min. Then, the mixture was transferred into a 50 mL Teflon-lined autoclave for synthesis at 170 °C for 3 days. The solids prepared were centrifuged, washed with DI water several times, and then dried at 110 °C in the oven overnight. Finally, the obtained sample was calcined in a muffle furnace at 550 °C for 6 h (1 °C min^{-1}) to remove the organic precursor and template. The resulting sample is denoted as 5Ni@EDA-S1.

2.1.6. Seed-directed synthesis of encapsulated Ni in S-1 catalyst (Ni@SiO_2-S1)

2.1.6.1. Preparation of Ni/SiO_2 seeds. SiO_2 seeds were synthesised by a modified Stöber method [25]. Specifically, 12 mL of TEOS was added dropwise into a water/ethanol mixture (24 mL and 160 mL, respectively) under stirring. Thereafter, 5 mL of $NH_3{\cdot}H_2O$ was added dropwise into the mixture for further reaction for 7 h. Finally, spherical SiO_2 seeds were centrifuged, washed with water for 3 times, and then dried at 80 °C in an oven overnight. Next, 1.0 g of SiO_2 seeds were dispersed into 60 mL of H_2O and then, $Ni(NO_3)_2{\cdot}6H_2O$ (0.5 g) and urea (molar ratio of NH_3/Ni = 10:1) were dissolved into 15 mL of H_2O to form nickel ammonia complex. Subsequently, the nickel ammonia complex was added to the silica dispersion and continued to be stirred for 2 h. The mixture was then transferred to the Teflon-lined autoclave and kept at 150 °C for 24 h. The resulting precipitate was centrifuged and washed with DI water to remove the ammonium ions.

2.1.6.2. Preparation of Ni@SiO_2-S1 catalyst. The catalyst was synthesised with the molar composition of SiO_2: TPAOH: H_2O (1:0.4:35). Typically, 1.0 g of the above-prepared Ni/SiO_2 seeds were dispersed in 17 mL of water by sonication for 1 h. Then, TPAOH solution (6.25 g) was added under stirring for 2 h. After that, 2.5 g of TEOS was added into the solution slowly, and the resulting solution was continuously stirred for 6 h to fully hydrolyse TEOS. Subsequently, the resulting gel was transferred into a 50 mL Teflon-lined autoclave for hydrothermal synthesis at 170 °C for 2 days. The obtained solid was washed with water and ethanol for several times, and then dried at 110 °C overnight, followed by calcination in air at 550 °C for 6 h. The obtained catalyst is denoted as 5Ni@SiO_2-S1.

2.2. Catalysis

Catalytic DRM was performed in a continuous flow fixed-bed reactor at atmospheric pressure (Figure S1). Typically, 60 mg of catalyst (pelletised to give particle sizes of 250–425 μm) was loaded in the centre of the reactor between two quartz wool plugs. The temperature of the catalyst bed was measured by a K-type thermocouple embedded in the catalyst bed. Before reaction, the catalyst was reduced at 700 °C for 1 h with 40 vol% H_2/Ar (at 100 mL min^{-1}). After reduction, the catalyst was cooled down to 500 °C in Ar (50 mL min^{-1}). Subsequently, the gas mixture of CO_2, CH_4 and Ar (molar ratio of 1:1:2) with a total flow rate of 50 mL min^{-1} was fed into the reactor (via three mass flow controllers, Bronkhorst®, F-201CV-500-RAD-11-V). The activity of the catalysts was measured between 500 and 750 °C at 50 °C intervals under steady state conditions. The stability of the catalysts was assessed at 700 °C with different durations (*i.e.,* time-on-stream, ToS, up to 28 h). The outlet gas composition was detected by a two-channel in-line gas chromatography (GC) equipped with an Elite-Carbon molecular sieve packed column (N 9303926), a thermal conductivity detector (TCD) and a flame ionisation detector (FID). For each measurement, three consecutive measurements of gas products were analysed to obtain the averaged values (error margins < 3%). The liquid products (*e.g.,* water) were removed by a glass water trap cooled by an ice bath and the total flowrate of the gas products was measured by a bubble-flow meter for the calculation of CO_2 conversion (X_{CO_2}, Eq. (1)) and CH_4 conversion (X_{CH_4}, Eq. (2)) and the H_2/CO molar ratio (Eq. (3)).

$$X_{CO_2} = \frac{F^{in}_{CO_2} - F^{out}_{CO_2}}{F^{in}_{CO_2}} \times 100 \quad (1)$$

$$X_{CH_4} = \frac{F^{in}_{CH_4} - F^{out}_{CH_4}}{F^{in}_{CH_4}} \times 100 \quad (2)$$

$$\frac{H_2}{CO} = \frac{F^{out}_{H_2}}{F^{out}_{CO}} \quad (3)$$

where F stands for the molar flow rate in the inlet (superscript in) and outlet (superscript out) of the reactor (mol s^{-1}).

Specific reaction rates for CO_2 and CH_4 conversions were calculated:

$$r_{CO_2/CH_4} = \frac{X_{CO_2/CH_4} \times F^{in}_{CO_2/CH_4}}{W_{cat.} \times X_{Ni}} \quad (4)$$

where r_{CO_2/CH_4} are the specific reaction rates of CO_2/CH_4 (mol s^{-1} g^{-1}), $W_{cat.}$ is the mass of catalyst used (g_{cat}), X_{Ni}(g_{Ni} g^{-1}_{cat}) is the Ni content in catalyst (as shown in Table 1).

3. Results and discussion

3.1. Physiochemical properties of catalysts.

Comparative XRD patterns of the calcined catalysts are presented in Fig. 1. The characteristic peaks of silicalite-1 at 2θ = 7.97°, 8.83°, 23.17°, 24.09° and 24.48°, corresponding to the (011), (200), (501), (033) and (133) facets, were observed for all the catalysts, proving the well-crystallised MFI structure (JCPDS no. 44–0696) [26]. In addition to the strong diffraction peaks of S-1 zeolite, diffraction peaks at about 2θ = 43.5° were also identified in the XRD patterns of 5Ni/S-1 and 5Ni@hol S-1, corresponding to the (200) facets of NiO (JCPDS no. 47–1049). Conversely, diffraction peaks of NiO phase were not observed in 5Ni@EDA-S1 and 5Ni@SiO_2-S1, suggesting the possible presence of highly dispersed NiO or encapsulated NiO [27,28]. The relative crystallinity of 5Ni/S-1, 5Ni@hol S-1 and 5Ni@EDA-S1 catalysts were decreased by 19.8%, 3.3%, and 17.7%, respectively, compared with parent S-1 zeolite, while the 5Ni@SiO_2-S1 catalyst has the comparable crystallinity with S-1 zeolite (calculated by XRD in Table S2), indicating that introducing Ni into zeolite by various methods affected the crystallinity of zeolite [26].

The morphology of the calcined catalysts is shown in Fig. 2. 5Ni/S-1 has an ellipsoid-shape morphology with an average crystal size of 240 nm. For 5Ni@hol S-1, broken zeolite crystals were found by SEM, showing the cavities, which confirm the formation of hollow structures. The average crystal size of 5Ni@hol S-1 was measured to be ~ 280 nm, and some large crystals were observed, which could be ascribed to the dissolution of the interior of S-1 zeolite and recrystallisation on its outer surface during the TPAOH treatment. 5Ni@EDA-S1 and 5Ni@SiO_2-S1 show a similar coffin-like morphology with larger crystal sizes than that of the catalyst prepared by impregnation. Specifically, for 5Ni@EDA-S1, the average crystal length was ~ 4.7 μm and some nanosheets were formed (as indicated in Fig. 2c), which can be the result of adding the [Ni($NH_2CH_2CH_2NH_2$)$_3$](NO_3)$_2$ precursor in the synthesis mixture, affecting the nucleation and crystallisation process of S-1 zeolite [29]. In contrast, 5Ni@SiO_2-S1 showed the well-defined crystal with an average length of ~ 3.1 μm, suggesting that the seed-directed synthesis method was beneficial to the formation of S-1 zeolite with uniform structure.

Microscopic details of the morphology and size distribution of NiO NPs of the calcined catalysts were further investigated by HRTEM, and the results are shown in Fig. 3. For 5Ni/S-1, NiO NPs with an average particle size of ~ 3.7 nm are distributed randomly on the external surface of S-1 crystals (Fig. 3a-c). After the TPAOH treatment, 5Ni@hol S-1 with a hollow structure and thin intact shell (average thickness of ~ 14 nm) was formed due to the dissolution-recrystallisation of 5Ni/S-1 during the post-treatment (Fig. 3d-f) [30], which is in line with the findings by SEM. Most of the Ni species migrated from the surface into the cavities, and thus are encapsulated by the shells of hollow S-1. The average NiO particle size of 5Ni@hol S-1 was comparable to that of 5Ni/S-1, indicating metal agglomeration was unlikely during the treatment. However, some NiO NPs were found anchored and/or remained on the outer surface of the cavities (as identified in Fig. 3d-e), which tended to

Table 1
Properties of the calcined 5Ni/S-1, 5Ni@hol S-1, 5Ni@EDA-S1 and 5Ni@SiO_2-S1 catalysts.

Catalyst	Actual Ni loading (%)[a]	Dispersion (%)[b]	S_{BET} ($m^2\ g^{-1}$)[c]	V_{total} ($cm^3\ g^{-1}$)[d]	V_{micro} ($cm^3\ g^{-1}$)	V_{meso} ($cm^3\ g^{-1}$)	Ni_{2p}/Si_{2p} ratio (%)[e]
5Ni/S-1	4.25	1.8	406	0.290	0.043	0.247	8.74
5Ni@hol S-1	6.28	4.5	417	0.413	0.034	0.379	1.61
5Ni@EDA-S1	4.09	21.9	428	0.350	0.039	0.311	2.75
5Ni@SiO_2-S1	4.23	23.5	401	0.284	0.024	0.26	0.79

[a] determined by ICP-OES. [b]because the CO adsorption is hindered on the reduced encapsulated catalyst (Figure S5), the Ni dispersion was calculated using average particle sizes of the reduced catalysts based on TEM (Supporting Information). [c]determined by the BET method. [d]single point adsorption total pore volume at $p/p_0 = 0.99$. [e]molar ratio of Ni to Si on the surface according to XPS.

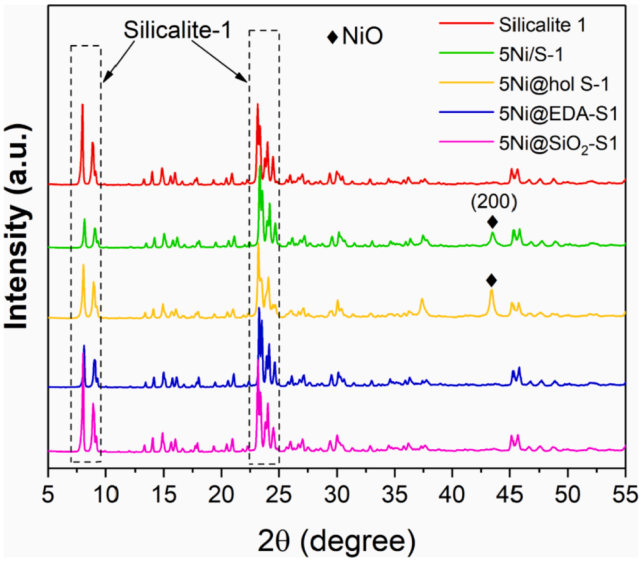

Fig. 1. XRD patterns of the as-prepared catalysts (after calcination in air at 550 °C for 6 h).

agglomerate into large particles. For 5Ni@EDA-S1, HRTEM images (Fig. 3g-i) showed that NiO NPs encapsulated within S-1 zeolite are uniformly dispersed and distributed throughout S-1 crystals, which is in line with the findings of previous studies [24,31]. However, some NiO NPs were found to be formed on the external surface of zeolite, which might be due to Ni precursors used in the synthesis leading to Ni growth on the internal and external surface of zeolite [32] (Figure S2), forming the partially encapsulated Ni structure (Figure S3a-d). By contrast, EDX of 5Ni@SiO_2-S1 catalyst in Figure S3f showed insignificant Ni species on the surface of the support, confirming that Ni particles are indeed fully encapsulated within S-1 crystals. Previous studies demonstrated that a 7 nm minimum threshold for Ni particle size is required for filamentous carbon formation [33]. Thus, the particle size distribution of 5Ni@SiO_2-S1 showed a comparatively small average NiO nanoparticle size of ~ 2.9 nm which may contribute to the catalyst preventing carbon deposition during DRM [34].

As shown from Table 1, all catalysts had surface areas of > 400 $m^2\ g^{-1}$ and pore volumes of > 0.28 $cm^3\ g^{-1}$. N_2 physisorption isotherms of the catalysts (Figure S4) showed a significant increase at relative pressure (p/p_0) of < 0.02 due to the micropore filling by N_2 molecules, confirming the presence of microporous structure in them regardless of their structures. Additionally, a type-IV N_2 adsorption–desorption isotherm with the H_4 type hysteresis loop was measured for 5Ni@hol S-1, 5Ni@EDA-S1 and 5Ni@SiO_2-S1, respectively, suggesting the presence of mesoporous structures. The corresponding average micropore and mesopore sizes were calculated to be 0.56 and 1.6–2.0 nm, respectively. Specifically, the hysteresis loops with an abrupt step at around $p/p_0 = 0.45$ in 5Ni@hol S-1 becomes more pronounced, which proves the hollow structure of S-1 crystals and suggests that the large internal voids are connected to the external surface through channels of ~ 2 nm [30], which is consistent with the TEM results.

The metal-support interaction is an important factor determining the catalytic performance, and thus, H_2-TPR analysis was performed to investigate the interactions between Ni and S-1 support, as shown in Fig. 4 and Table S3. Only one reduction peak centered at 431 °C was observed in 5Ni/S-1 and was assigned to the reduction of NiO on the external surface of S-1, indicating that the conventional impregnation method was not able to introduce Ni NPs into the zeolite. In comparison, the major reduction peak at 461 °C for 5Ni@hol S-1 can be ascribed to the reduction of encapsulated NiO in hollow S-1, suggesting that the encapsulation *via* TPAOH treatment could strengthen the interaction between Ni and S-1 support as compared with the impregnated 5Ni/S-1 [27]. Regarding 5Ni@EDA-S1, the peak at 350 °C was attributed to the reduction of NiO species weakly interacted with the support, whilst the reduction peak at high temperatures (732–737 °C) can be related to the NiO particles embedded in S-1 with strong metal-support interactions caused by the confinement effect [18]. Additionally, the broad reduction peaks from 426 to 615 °C in 5Ni@SiO_2-S1 are associated with the reduction of the encapsulated NiO species with relatively smaller particle sizes [15,18], being consistent with the Ni sizes found via TEM analysis. The results above suggest a relatively strong metal-support interaction in 5Ni@EDA-S1 and 5Ni@SiO_2-S1, which can potentially improve the anti-sintering ability of Ni during catalysis, thus benefiting DRM [35].

XPS analysis was performed to evaluate the chemical state of Ni species in the catalysts under investigation, and the results are shown in Fig. 5. The high-resolution XPS spectra of Ni 2p was deconvoluted into two Ni $2p_{3/2}$ peaks at 855.6 eV attributed to Ni^{2+} in NiO, and at 861.5 eV associated with the satellite peaks of Ni^{2+}. It was found that Ni 2p spectra shifted to higher binding energy in the following order: 5Ni/S-1 < 5Ni@hol S-1 < 5Ni@EDA-S1 < 5Ni@SiO_2-S1. Such findings indicate the relatively strong interactions between encapsulated Ni NPs and S-1 support [27,36], which is consistent with the H_2-TPR results. Relative XPS intensity can be used to calculate the surface concentration of Ni in a catalyst [26]. As shown in Table 1, 5Ni/S-1 showed the highest Ni 2p/Si 2p intensity ratio, suggesting that the Ni was mainly located on the external surface of S-1. Comparatively, the ratios were 1.61 and 2.75 for 5Ni@hol S-1 and 5Ni@EDA-S1, respectively, which confirm the co-existence of Ni on the external and internal surface of S-1 and is consistent with TEM results. 5Ni@SiO_2-S1 had the lowest ratio of 0.79, which suggests that Ni species were fully encapsulated inside S-1.

3.2. Catalytic performance of the catalysts in DRM.

Catalytic DRM over the catalysts under investigation was first evaluated in the temperature range from 500 to 750 °C to compare their performance regarding the CO_2/CH_4 conversions and H_2/CO molar ratio. As shown in Fig. 6, for all the catalysts, the CO_2 and CH_4 reaction rates increased progressively as a function of reaction temperature, as expected (Fig. 6a and b). Specifically, the impregnated 5Ni/S-1 catalyst showed the highest CO_2/CH_4 conversion rates due to the easy accessibility of Ni active sites on its external surface, whilst the 5Ni@hol S-1 catalyst presented the lowest activity, which might be caused by the

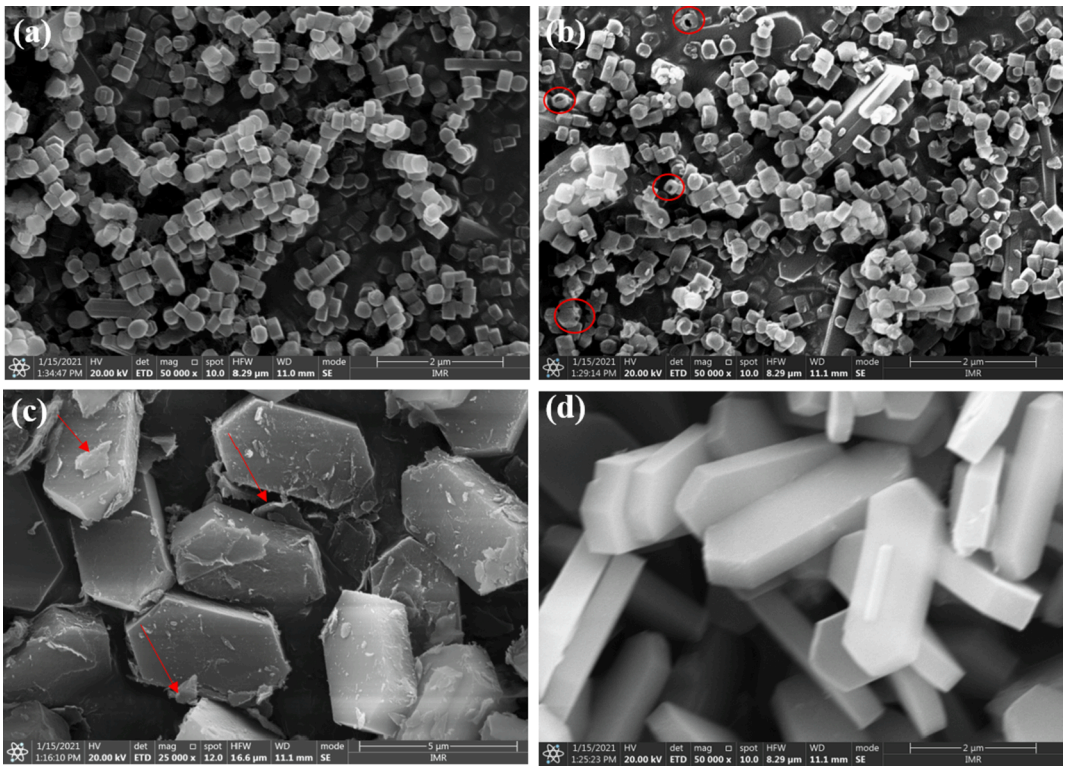

Fig. 2. SEM micrographs of the calcined (a) 5Ni/S-1, (b) 5Ni@hol S-1, (c) 5Ni@EDA-S1 and (d) 5Ni@SiO_2-S1 catalysts.

diffusion and transport resistance of the reactants to Ni NPs in the cavity through the channels of the S-1 shell. The 5Ni@SiO_2-S1 catalyst showed slightly better performance than 5Ni@EDA-S1 over the temperature range investigated. Specifically, the CO_2/CH_4 conversions over 5Ni@SiO_2-S1 increased from ~ 29.7% and ~ 22.0%, respectively, at 550 °C to ~ 83.7% and ~ 82.2% at 750 °C (Fig. 6d). All catalysts showed very low initial values of H_2/CO molar ratio, *i.e.*, < 0.5 at 550 °C. This low amount of H_2 formed is attributed to the presence of the reverse water–gas shift reaction [37,38]. Thus, 5Ni@SiO_2-S1 showed higher conversion of CO_2 (~29.7%) than that of CH_4 (~22.0%) at low temperature of 550 °C (Fig. 6d). The H_2/CO ratio of all catalysts increased rapidly by an increase of the temperature, which is due to the increased H_2 production *via* DRM and/or the encouraged methane cracking reaction at high temperatures (*i.e.,* $CH_4 \rightarrow C + 2H_2$, $\Delta H^{\circ}_{298K} = +74.9$ kJ mol^{-1}). Accordingly, the carbon balance of the reaction over all the catalysts (Figure S8) decreased progressively as a function of reaction temperature, suggesting carbon and H_2 formation is promoted from CH_4 decomposition at high reaction temperatures [39]. Theoretically, the H_2/CO molar ratio is expected to be unity, whereas in this work, the highest value obtained by the catalysts was around 0.9 at 700 °C (for 5Ni@SiO_2-S1), suggesting the possible occurrence of RWGS [40].

Longevity tests were performed to understand the effect of different catalyst structures on coke deposition and associated catalyst deactivation. The tests were performed over the four catalysts under study at 600 °C and 700 °C, and the results are shown in Figure 7 and S9. As shown in Fig. 7, the impregnated 5Ni/S-1 catalyst suffered from a significant deactivation after start-up, *i.e.,* CO_2/CH_4 conversions dropped by 28% and 39%, respectively, and the molar ratio of H_2/CO decreased from 0.9 to 0.78 over 8 h on stream. Similarly, the 5Ni@hol S-1 catalyst also deactivated in DRM though the encapsulation of Ni NPs in hollow S-1 were created by the TPAOH treatment, which was aimed at sustaining the activity of 5Ni@hol S-1 by preventing coking and metal sintering. More importantly, the DRM process over the two catalysts halted after 8 h on stream due to physical blocking of the packed bed (with measured back pressure of > 2.0 bar), which was caused by significant coke formation within the reactor. Comparatively, 5Ni@hol S-1 showed a relatively improved stability (*i.e.,* relevant deactivation by 23% and 13% for CO_2/CH_4 conversions over 8 h on stream, respectively). Additionally, the TGA profile in Fig. 7d showed that the spent 5Ni/S-1 catalyst (after 8 h DRM on stream at 700 °C) presented a significant weight loss of ~ 27.4% between 500 and 750 °C. In contrast, the used 5Ni@hol S-1 catalyst showed a lower weight loss of ~ 9.2%, which confirmed that encapsulation could suppress the carbon deposition during DRM to some extents. For the reduced 5Ni/S-1 catalyst, TEM analysis showed significant aggregation of Ni NPs (with average particle size of ~ 56.7 nm) after reduction, which might accelerate coking during DRM (Fig. 8a). It was found that carbon deposition in the spent 5Ni/S-1 catalyst is considerable, which caused deactivation of the catalyst (Fig. 8b and S10a). Comparatively, even though the hollow zeolite shell in 5Ni@hol S-1 catalyst was reported to be able to inhibit Ni sintering and coking [22], the Ni NPs, which were not encapsulated in the hollow S-1 crystals, were found aggregated into the large particles (with average particle size of ~ 59.2 nm) during the reduction treatment (as shown in Fig. 8c), which could lead to the formation of carbon intermediates and their continuous accumulation of coke on the external catalyst surface (Fig. 8d and S10b). The carbon deposition contributed to the reduced accessibility of Ni active sites to reactant gases, leading to the reduced CO_2/CH_4 conversions for DRM. Therefore, coke deposition on 5Ni@hol S-1 was still inevitable in a long run due to the incomplete encapsulation of Ni NPs in its structure. However, the Ni NPs encapsulated within hollow S-1 (with average particle size of ~ 3.8 nm) remained active due to the confinement effect (as indicated in Fig. 8d), leading to an improved coke-resistance compared to 5Ni/S-1. It is also worth mentioning that the over-spacious interior cavity in 5Ni@hol S-1 could possibly reduce the confinement effect of the S-1 support on Ni NPs, causing the possible migration/aggregation of Ni NPs inside the cavity at high temperatures (as indicated in Figure S11), which may lead to the interparticle combination/growth and thus impair the anti-coking capacity of the catalyst [15,41].

5Ni@EDA-S1 presented a relatively low initial activity, which

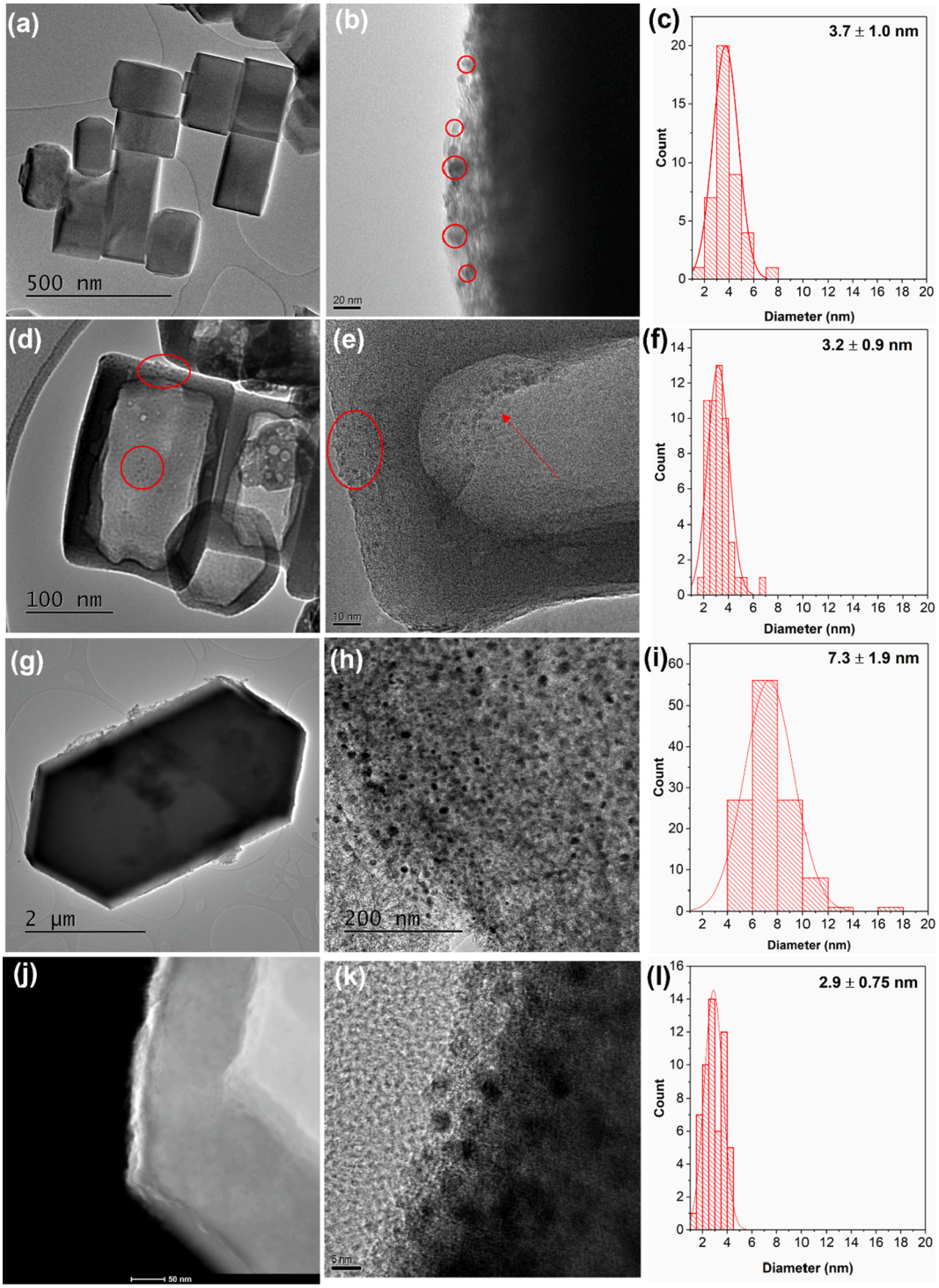

Fig. 3. HRTEM images and corresponding Ni particle size distribution of (a–c) 5Ni/S-1, (d–f) 5Ni@hol S-1, (g–i) 5Ni@EDA-S1 and (j–l) 5Ni@SiO_2-S1 (after calcination).

increased gradually within the first 5 h on stream and remained stable, that is, the CO_2/CH_4 conversions and H_2/CO molar ratio increased from 67%, 53% and 0.73 to 72%, 64% and 0.85, respectively. HRTEM results in Figure S3 showed that some Ni NPs exposed on the external surface in 5Ni@EDA-S1 might be prone to aggregate into large particles at high reaction temperatures. However, a previous study on the effect of particle sizes on DRM over the Ni/SiO_2 catalyst demonstrated that the activity of DRM decreased with an increase in Ni particle sizes [10]. Thus, the aggregation of Ni NPs on the external surface of 5Ni@EDA-S1 was not responsible for this increasing trend measured in the first 5 h. STEM images and elemental analysis of the reduced and spent 5Ni@EDA-S1catalyst (Fig. 8e, S12 and S14) show that some Ni NPs, which were located inside of the S-1 support, migrated out of framework to the external surface at high temperatures, especially to the edge of zeolite, leading to more active sites exposed on the external surface and contributing to the stable CO_2/CH_4 conversions. However, these Ni NPs may encourage the coke formation on their surfaces (Fig. 8f and S12b). Comparatively, at the lower reaction temperature of 600 °C (Figure S9),

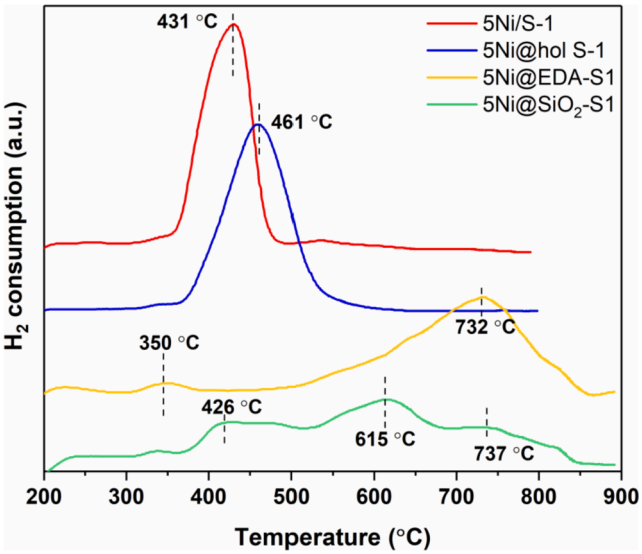

Fig. 4. H_2-TPR profiles of the calcined catalysts.

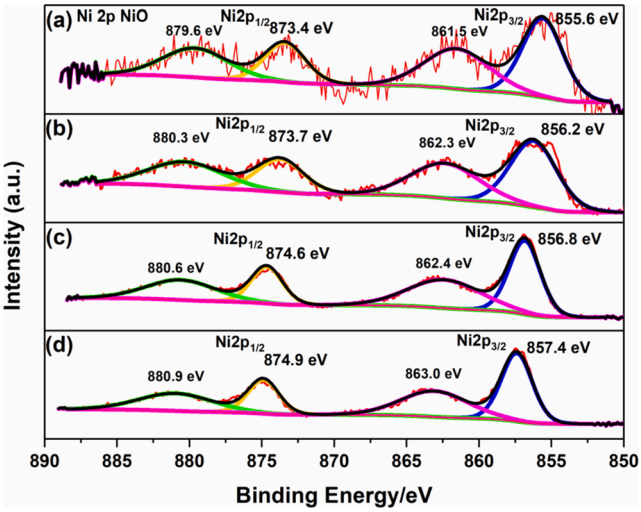

Fig. 5. Ni 2p photoelectron spectra of different catalysts after calcination: (a) 5Ni/S-1, (b) 5Ni@hol S-1, (c) 5Ni@EDA-S1 and (d) 5Ni@SiO_2-S1.

CO_2/CH_4 conversions decreased from 51% and 54% to 42.7% and 41.2%, respectively, over 5Ni@EDA-S1, which may be caused by limited migration of Ni and reduced active sites due to coking. The corresponding TGA profile of the spent 5Ni@EDA-S1 (Fig. 7d) shows a 2.5% weight loss (suggesting the combustion of deposited coke), which lead to the physical blockage of the packed bed at 16 h during the stability test. Additionally, TEM analysis of the spent 5Ni@EDA-S1 in Fig. 8f shows the formation of filamentous carbon. The corresponding temperature-programmed oxidation of the spent 5Ni@EDA-S1 catalyst (Figure S13) showed the peak of CO_2 emission at ~ 673 °C, indicating that the coke requires high temperature to be oxidized, which is in line with the TGA result. The corresponding elemental mapping of spent catalyst in Figures S14h and S16c show the relatively uniform distribution of Ni species on the surface of the spent 5Ni@EDA-S1, suggesting the migration of Ni to the external surface. However, in comparison with large cavities in 5Ni@hol S-1, the surrounding interconnected framework of S-1 shell in 5Ni@EDA-S1 could provide sufficient isolation for the encapsulated Ni NPs (with strong metal-support interactions, as shown in Fig. 4), which reduced the accumulation of carbon on the Ni surface [15,41]. This also contributed to the sustained CO_2/CH_4 conversions without deactivation throughout the 16 h longevity test, demonstrating the improved resistance of the 5Ni@EDA-S1 catalyst to deactivation compared to 5Ni@hol S-1.

Comparatively, the 5Ni@SiO_2-S1 catalyst showed the best stability in DRM among the catalysts under investigation, with a sustained high activity (~80% and ~ 73% for CO_2/CH_4 conversions, respectively) over 28 h and a stable H_2/CO molar ratio of 0.83 with negligible carbon deposition (~0.5% based on TGA, as shown in Fig. 7d). In comparison with 5Ni@EDA-S1, the corresponding STEM images and elemental mapping of the reduced 5Ni@SiO_2-S1 (indicated in Fig. 8g, S12 and S15a-d) show insignificant migration of Ni NPs from the inside of the zeolite, *i.e.,* the full encapsulation structure was intact after reduction. Thus, the spent 5Ni@SiO_2-S1 catalyst showed insignificant carbon formation on the external surface after 28 h on stream. As shown in Fig. 8h and S15e–h, although it is still inevitable that Ni NPs migrated to the external surface of the support in a long run due to the high reaction temperature, the presence of Ni species on the external surface of the spent 5Ni@SiO_2-S1 catalyst was significantly lower than that of the spent 5Ni@EDA-S1 (Figure S16f). Therefore, the 5Ni@SiO_2-S1 catalyst prepared by seed-directed synthesis demonstrated comparatively good activity, anti-sintering and anti-coking abilities in DRM.

The chemical states of Ni species in all the catalysts were further investigated by XPS. For reduced catalysts (Figure S17), the surface Ni NPs show oxidation due to air exposition at RT after reduction and Ni 2p peaks were deconvoluted into Ni^{2+} and Ni^0 [42]. It can be seen that the binding energy of Ni 2p spectra for Ni^{2+} shifted to higher binding energy in the following order: 5Ni/S-1 < 5Ni@hol S-1 < 5Ni@EDA-S1 < 5Ni@SiO_2-S1, which is consistent with that of calcinated catalysts. An additional Ni^0 peak appeared in the 5Ni@EDA-S1 and 5Ni@SiO_2-S1 catalysts, confirming the improved reduction level of Ni species in the two encapsulated structures. Additionally, the XPS spectra (Figure S18) of spent 5Ni/S-1 and 5Ni@hol S-1 showed no Ni-related peaks, which can be attributed to the severe coking deposition on the surface, while it can be observed for the spent 5Ni@EDA-S1 and 5Ni@SiO_2-S1, being consistent with TGA and TEM results.

Fig. 9 shows the X-ray diffraction patterns of the reduced and spent catalysts (after stability tests). The diffraction patterns of all the S-1 supports were comparable to that of the pristine S-1, which confirms the stability of the supports during the reaction. Also, the characteristic peaks of Ni^0 at 44.45° and 51.9° in the reduced and spent 5Ni/S-1, 5Ni@hol S-1 and 5Ni@EDA-S1 were observed, showing the presence of large metallic Ni NPs on the external surface of catalysts, whilst Ni^0 phase was not detected in the reduced/spent 5Ni@SiO_2-S1, suggesting highly dispersed Ni in the fully encapsulated structure and negligible metal sintering, which is consistent with the TEM results above. Additionally, a new peak at 26.1°, corresponding to graphitic carbon (JCPDS card 12–0212), can be observed in the spent 5Ni/S-1 and 5Ni@hol S-1, whilst it was not detected for the spent 5Ni@EDA-S1 and 5Ni@SiO_2-S1 due to insignificant carbon deposition, which is consistent with the TGA results.

Based on the results, the reduced 5Ni/S-1 and 5Ni@hol S-1 catalysts suffered from Ni aggregation/sintering with large Ni particles formed during the reduction treatment. For the reduced 5Ni@EDA-S1 catalyst, some small Ni NPs migrated to the external surface of zeolite, especially to the edge of zeolite after reduction, which might in turn aggregate into large particles to encourage coke formation on their surfaces. Comparatively, for the reduced 5Ni@SiO_2-S1 catalyst, Ni aggregation is negligible, and the full encapsulation structure was intact after reduction. Thus, a number of factors are likely to influence the anti-coking mechanism of the 5Ni@SiO_2-S1 catalyst, including (i) small Ni NPs (~2.9 nm) could inhibit coke deposition on their surface, since the nucleation process of the filamentous carbon was suppressed over the small Ni particles of < 7 nm [43], (ii) fully encapsulated Ni NPs in the S-1 framework with strong metal-support interactions (*i.e.,* completely encapsulated Ni NPs within the S-1 framework) could impede the movement/aggregation of Ni NPs (due to the confinement incurred by

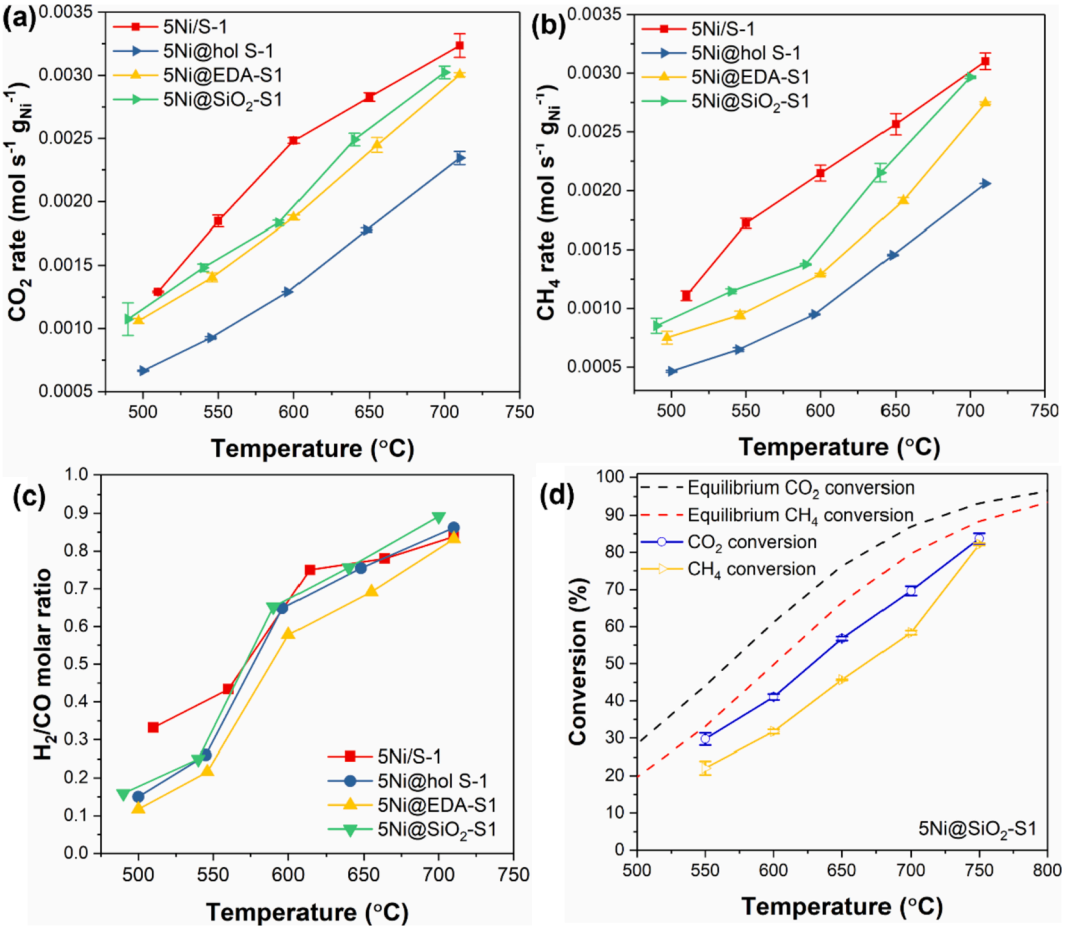

Fig. 6. (a) CO_2 conversion rate, (b) CH_4 conversion rate, (c) H_2/CO molar ratio as a function of temperature over different catalysts and (d) Equilibrium CO_2/CH_4 conversion, and CO_2 and CH_4 conversions as a function of temperature over 5Ni@SiO_2-S1. (reaction conditions: catalyst = 60 mg, GHSV = 750 L h^{-1} g_{Ni}^{-1}, CO_2/CH_4/Ar = 1:1:2).

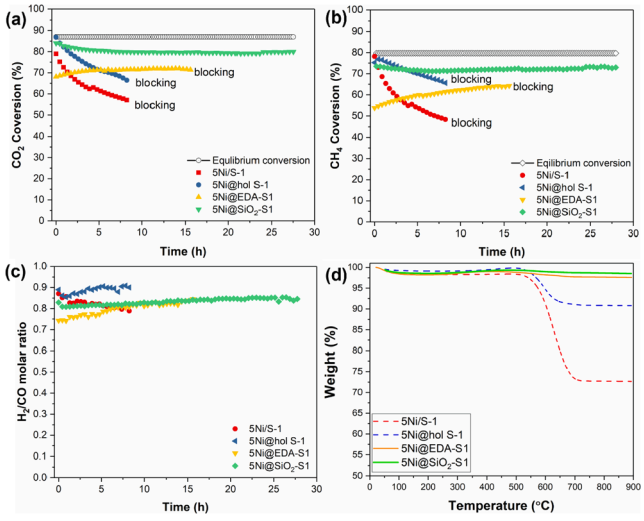

Fig. 7. Catalytic stability performances of 5Ni/S-1, 5Ni@hol S-1, 5Ni@EDA-S1 and 5Ni@SiO_2-S1 in DRM at 700 °C as a function of ToS: (a) CO_2 conversion, (b) CH_4 conversion and (c) H_2/CO molar ratio; (d) TGA profiles of the spent catalysts after stability testing (reaction conditions: catalyst = 80 mg, T = 700 °C, GHSV = 750 L h^{-1} g_{Ni}^{-1}, CO_2/CH_4/Ar = 1:1:2) (blocking: physical blocking of the packed bed with the measured back pressure > 2.0 bar).

the surrounding zeolite framework), and (iii) the walls of interconnected porous zeolite framework provide steric physical barriers against the spatial growth and accumulation of coking, maintaining enough active sites for reaction in DRM [41]. Therefore, carbon deposition could be mitigated by the encapsulation approach (*i.e.,* partially/completely encapsulated metal NPs within S-1). However, the intrinsic nature of encapsulated Ni catalysts prepared by different methods such as metal particle size, degree of encapsulation, zeolite shell structure and metal-support interactions, significantly affect the catalytic performance in terms of the metal sintering and carbon deposition in DRM. A corresponding structure-performance of each catalyst was proposed, as shown in Fig. 10.

Based on the activity tests above, encapsulated catalysts presented relatively stable CO_2/CH_4 conversions at 700 °C compared with the impregnated 5Ni/S-1 catalyst. However, as illustrated in Fig. 10, CO_2/CH_4 must penetrate through the zeolite shell to be activated and react on Ni sites. Simultaneously, the products of H_2 and CO need to escape from the shell again. Thus, the effect of mass-transfer resistance during DRM deserves further investigation. Accordingly, DRM at different GHSV was performed, and the results are shown in Fig. 11. When GHSV increased from 750 to 3000 L h^{-1} g_{Ni}^{-1} (total flowrate increased from 50 to 200 mL min^{-1}), CO_2 and CH_4 conversions and H_2/CO molar ratio in the control 5Ni/S-1 catalyst (prepared by impregnation) decreased from ~ 84%, ~80% and ~ 0.78 to ~ 59%, ~54% and ~ 0.58, respectively. Comparatively, CO_2 and CH_4 conversions and H_2/CO molar ratio of the 5Ni@hol S-1 catalyst dropped significantly under the same conditions, *i.e.,* from ~ 72%, ~59% and ~ 0.76 to ~ 31%, ~20% and ~ 0.50, respectively. Similarly, 5Ni@EDA-S1 showed 50.4% and 56.5%

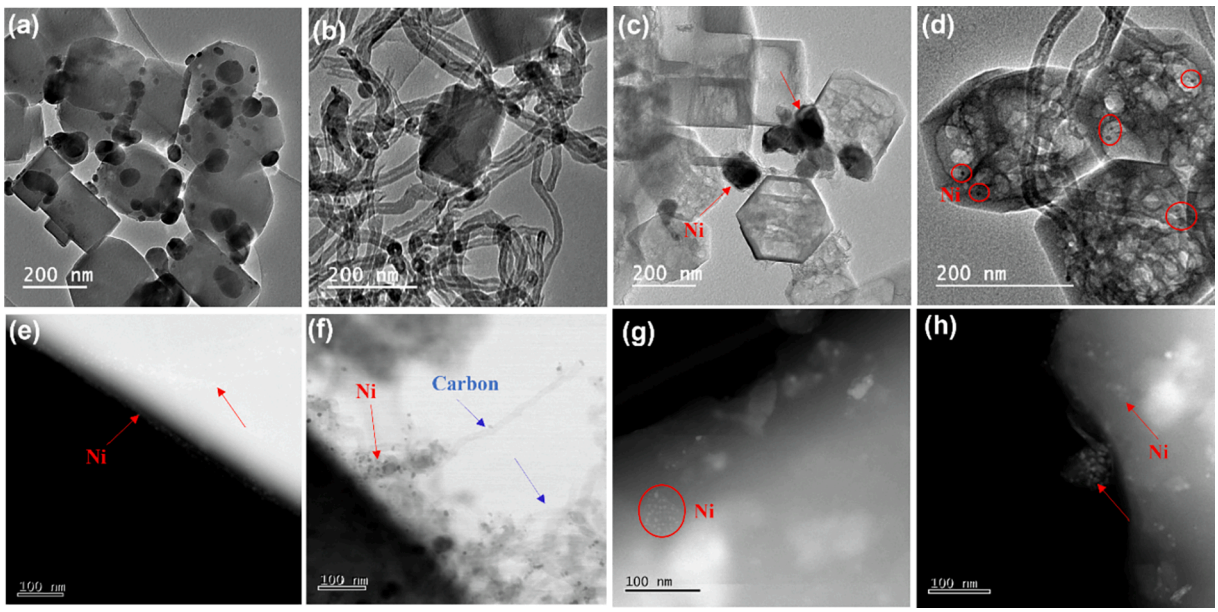

Fig. 8. TEM images (a-d) and ADF-STEM (e-h) of the catalysts after reduction at 700 °C and stability test at 700 °C. (a) 5Ni/S-1 after reduction, (b) spent 5Ni/S-1 after 8 h test, (c) 5Ni@hol S-1 after reduction and (d) spent 5Ni@hol S-1 after 8 h test, (e) 5Ni@EDA-S1 after reduction, (f) spent 5Ni@EDA-S1 after 16 h test, (g) 5Ni@SiO_2-S1 after reduction and (h) spent 5Ni@SiO_2-S1 after 28 h test.

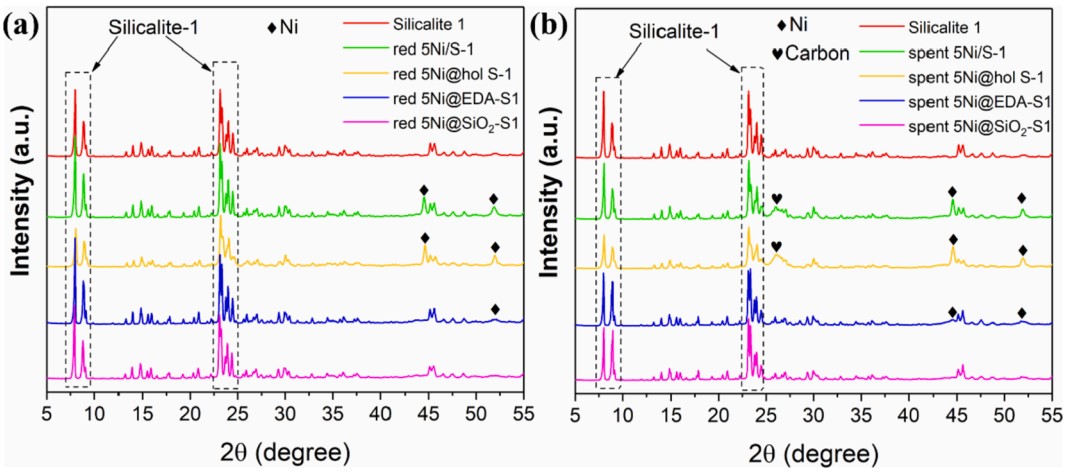

Fig. 9. XRD patterns of (a) the reduced catalysts (in H_2/Ar at 700 °C for 1 h) and (b) spent catalysts after stability test.

decrease in CO_2/CH_4 conversions, and a decrease of 43.1% and 52.9% were observed over 5Ni@SiO_2-S1. The findings suggest that the S-1 encapsulated Ni catalyst experienced relatively severe mass-transfer resistance as compared with 5Ni/S-1. Therefore, the trade-off between stability and mass-transfer resistance in the encapsulated catalysts needs to be considered carefully in the process of designing highly efficient catalysts for DRM.

4. Conclusions

In catalytic dry reforming of CH_4 with CO_2, rapid deactivation of Ni-based catalysts due to metal sintering and coking is a major challenge. In this study, a series of encapsulated Ni catalysts (by silicalite-1 zeolite) were prepared by different synthesis methods, and comprehensive characterisation revealed that their structural properties varied significantly, such as metal particle size, degree of encapsulation, and metal-support interactions, which affected their catalytic performance in DRM. It was demonstrated that, in general, the encapsulation strategy was effective to improve the stability of the resulting catalysts. However, the intrinsic nature of the catalysts developed by different methods played a key role in suppressing coking and Ni metal sintering during DRM. The developed Ni@SiO_2-S1 catalyst synthesized by a seed-directed synthesis method showed a complete encapsulation of Ni in its structure and the comparatively best catalytic performance with stable CO_2 and CH_4 conversions of ~ 80% and ~ 73%, respectively, as well as relatively low carbon deposition (about 0.5 wt% by TGA), after 28 h on stream, which outperformed other catalysts under investigation. Conversely, the post treatment and direct hydrothermal methods promoted the incomplete encapsulation of Ni (*i.e.,* the 5Ni@hol S-1 and 5Ni@EDA-S1 catalysts), being prone to deactivation due to the presence of Ni phases on their external surface. By contrast, the impregnated Ni catalyst (with Ni particles only on the external surface of S-1 support) suffered from rapid deactivation and severe carbon deposition after the 8 h test. Additionally, the severe mass transfer resistance of encapsulated catalysts needs to be further mitigated for the reaction.

This work aimed to understand the synthesis-structure-performance relationships of Ni-S-1 catalysts. Its findings show clearly that the full encapsulated Ni in the support with small Ni particle sizes and strong

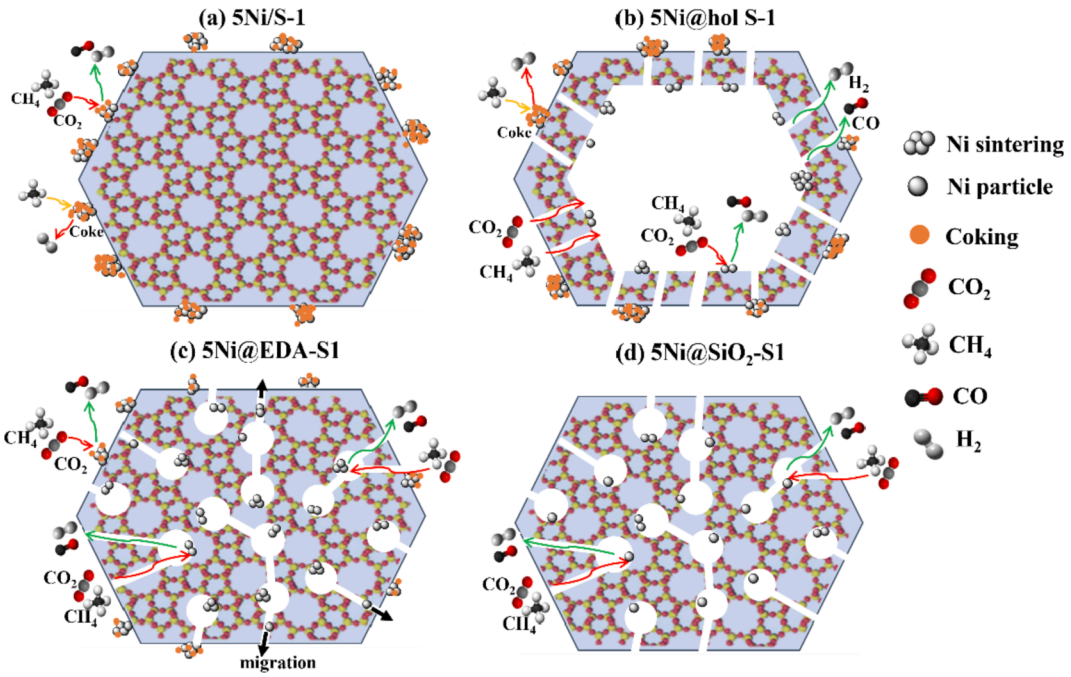

Fig. 10. Schematic illustration of DRM over the encapsulated catalysts with different structures regarding Ni aggregation and carbon deposition: (a) 5Ni/S-1, (b) 5Ni@hol S-1, (c) 5Ni@EDA-S1 and (d) 5Ni@SiO_2-S1.

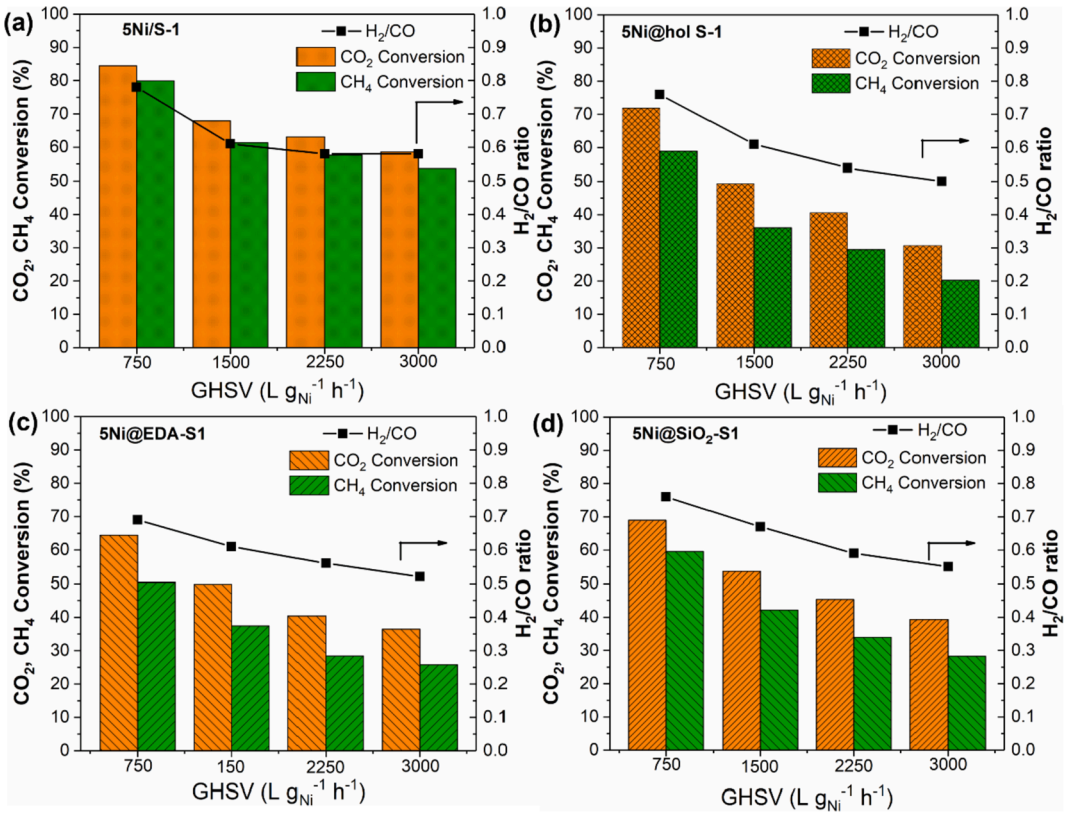

Fig. 11. Catalytic DRM performance as a function of hourly space velocity over (a) 5Ni/S-1, (b) 5Ni@hol S-1, (c) 5Ni@EDA-S1 and (d)5Ni@SiO_2-S1. (reaction conditions: catalyst = 60 mg, T = 700 °C, total flow rate = 50–200 mL min^{-1}, GHSV = 750–3000 L h^{-1} g_{Ni}^{-1}, $CO_2/CH_4/Ar$ = 1:1:2).

metal-support interactions in the Ni@SiO_2-S1 catalyst could protect Ni aggregation and inhibit coke formation during DRM, providing design rationales for developing stable metal-based catalyst with coking- and sintering-resistance for high-temperature heterogeneous catalysis such as DRM.

Declaration of Competing Interest

The authors declare that they have no known competing financial interests or personal relationships that could have appeared to influence the work reported in this paper.

Acknowledgments

SX thanks the financial supports from the Dean's Doctoral Scholar Awards from the University of Manchester. UK Catalysis Hub is kindly thanked for resources and support provided via our membership of the UK Catalysis Hub Consortium and funded by EPSRC grants: EP/R026939/1, EP/R026815/1, EP/R026645/1 and EP/R027129/1. We thank Diamond Light Source for access and support in use of the electron Physical Science Imaging Centre (Instrument E01 and proposal number MG29468) that contributed to the results presented here.

Appendix A. Supplementary data

Supplementary data to this article can be found online at https://doi.org/10.1016/j.cej.2022.137439.

References

[1] S. Subramanian, Y. Song, D. Kim, C.T. Yavuz, Redox and nonredox CO_2 utilization: Dry reforming of methane and catalytic cyclic carbonate formation, ACS Energy Lett. 5 (5) (2020) 1689–1700.
[2] W.-J. Jang, J.-O. Shim, H.-M. Kim, S.-Y. Yoo, H.-S. Roh, A review on dry reforming of methane in aspect of catalytic properties, Catal. Today 324 (2019) 15–26.
[3] Y. Lyu, J. Jocz, R. Xu, E. Stavitski, C. Sievers, Nickel speciation and methane dry reforming performance of $Ni/Ce_xZr_{1-x}O_2$ prepared by different synthesis methods, ACS Catal. 10 (19) (2020) 11235–11252.
[4] T. Stroud, T.J. Smith, E. Le Saché, J.L. Santos, M.A. Centeno, H. Arellano-Garcia, J. A. Odriozola, T.R. Reina, Chemical CO_2 recycling via dry and bi reforming of methane using $Ni-Sn/Al_2O_3$ and $Ni-Sn/CeO_2-Al_2O_3$ catalysts, Appl. Catal. B: Environ 224 (2018) 125–135.
[5] Y.e. Wang, L.u. Yao, Y. Wang, S. Wang, Q. Zhao, D. Mao, C. Hu, Low-temperature catalytic CO_2 dry reforming of methane on $Ni-Si/ZrO_2$ catalyst, ACS Catal. 8 (7) (2018) 6495–6506.
[6] Z. Xie, B. Yan, S. Kattel, J.H. Lee, S. Yao, Q. Wu, N. Rui, E. Gomez, Z. Liu, W. Xu, L. Zhang, J.G. Chen, Dry reforming of methane over CeO_2-supported Pt-Co catalysts with enhanced activity, Appl. Catal. B: Environ 236 (2018) 280–293.
[7] D.G. Araiza, D.G. Arcos, A. Gómez-Cortés, G. Díaz, Dry reforming of methane over $Pt-Ni/CeO_2$ catalysts: effect of the metal composition on the stability, Catal. Today 360 (2021) 46–54.
[8] Z. Liu, F. Zhang, N. Rui, X. Li, L. Lin, L.E. Betancourt, D. Su, W. Xu, J. Cen, K. Attenkofer, H. Idriss, J.A. Rodriguez, S.D. Senanayake, Highly active ceria-supported Ru catalyst for the dry reforming of methane: In situ identification of $Ru^{\delta+}$–Ce^{3+} interactions for enhanced conversion, ACS Catal. 9 (2019) 3349–3359.
[9] H. Peng, X. Zhang, X. Han, X. You, S. Lin, H. Chen, W. Liu, X. Wang, N. Zhang, Z. Wang, P. Wu, H. Zhu, S. Dai, Catalysts in coronas: A surface spatial confinement strategy for high-performance catalysts in methane dry reforming, ACS Catal. 9 (2019) 9072–9080.
[10] D. Baudouin, U. Rodemerck, F. Krumeich, A.d. Mallmann, K.C. Szeto, H. Ménard, L. Veyre, J.-P. Candy, P.B. Webb, C. Thieuleux, C. Copéret, Particle size effect in the low temperature reforming of methane by carbon dioxide on silica-supported Ni nanoparticles, J. Catal., 297 (2013) 27-34.
[11] R. Franz, T. Kühlewind, G. Shterk, E. Abou-Hamad, A. Parastaev, E. Uslamin, E.J. M. Hensen, F. Kapteijn, J. Gascon, E.A. Pidko, Impact of small promoter amounts on coke structure in dry reforming of methane over Ni/ZrO_2, Catal. Sci. Technol. 10 (12) (2020) 3965–3974.
[12] A.A. Abdulrasheed, A.A. Jalil, M.Y.S. Hamid, T.J. Siang, T.A.T. Abdullah, Dry reforming of CH_4 over stabilized Ni-La@KCC-1 catalyst: Effects of La promoter and optimization studies using RSM, J. CO2 Util. 37 (2020) 230–239.
[13] Z. Wu, B. Yang, S. Miao, W. Liu, J. Xie, S. Lee, M.J. Pellin, D. Xiao, D. Su, D. Ma, Lattice strained Ni-Co alloy as a high-performance catalyst for catalytic dry reforming of methane, ACS Catal. 9 (4) (2019) 2693–2700.
[14] T. Margossian, K. Larmier, S.M. Kim, F. Krumeich, C. Müller, C. Copéret, Supported bimetallic NiFe nanoparticles through colloid synthesis for improved dry reforming performance, ACS Catal. 7 (10) (2017) 6942–6948.
[15] C. Wang, X. Jie, Y. Qiu, Y. Zhao, H.A. Al-Megren, S. Alshihri, P.P. Edwards, T. Xiao, The importance of inner cavity space within $Ni@SiO_2$ nanocapsule catalysts for excellent coking resistance in the high-space-velocity dry reforming of methane, Appl. Catal. B: Environ 259 (2019) 118019.
[16] S. Das, J. Ashok, Z. Bian, N. Dewangan, M.H. Wai, Y. Du, A. Borgna, K. Hidajat, S. Kawi, Silica-Ceria sandwiched Ni core–shell catalyst for low temperature dry reforming of biogas: Coke resistance and mechanistic insights, Appl. Catal. B: Environ 230 (2018) 220–236.
[17] S.H. Joo, J.Y. Park, C.-K. Tsung, Y. Yamada, P. Yang, G.A. Somorjai, Thermally stable Pt/mesoporous silica core-shell nanocatalysts for high-temperature reactions, Nat. Mater. 8 (2) (2009) 126–131.
[18] T. Xie, L. Shi, J. Zhang, D. Zhang, Immobilizing Ni nanoparticles to mesoporous silica with size and location control via a polyol-assisted route for coking- and sintering-resistant dry reforming of methane, Chem. Commun. (Camb.) 50 (55) (2014) 7250–7253.
[19] F. Wang, B. Han, L. Zhang, L. Xu, H. Yu, W. Shi, CO_2 reforming with methane over small-sized $Ni@SiO_2$ catalysts with unique features of sintering-free and low carbon, Appl. Catal. B: Environ 235 (2018) 26–35.
[20] H. Wang, L. Wang, F.-S. Xiao, Metal@zeolite hybrid materials for catalysis, ACS Cent. Sci. 6 (10) (2020) 1685–1697.
[21] J. Zhang, L. Wang, B. Zhang, H. Zhao, U. Kolb, Y. Zhu, L. Liu, Y.u. Han, G. Wang, C. Wang, D.S. Su, B.C. Gates, F.-S. Xiao, Sinter-resistant metal nanoparticle catalysts achieved by immobilization within zeolite crystals via seed-directed growth, Nat. Catal. 1 (7) (2018) 540–546.
[22] C. Dai, S. Zhang, A. Zhang, C. Song, C. Shi, X. Guo, Hollow zeolite encapsulated Ni–Pt bimetals for sintering and coking resistant dry reforming of methane, J. Mater. Chem. A 3 (32) (2015) 16461–16468.
[23] T. Kobayashi, T. Furuya, H. Fujitsuka, T. Tago, Synthesis of Birdcage-type zeolite encapsulating ultrafine Pt nanoparticles and its application in dry reforming of methane, Chem. Eng. J. 377 (2019) 120203.
[24] B. Zhang, Y. Tian, D. Chen, L. Li, G. Li, L. Wang, X. Zhang, G. Liu, Selective steam reforming of n-dodecane over stable subnanometric NiPt clusters encapsulated in Silicalite-1 zeolite, AIChE J. 66 (2020) 16917.
[25] K.M. Kwok, S.W.D. Ong, L. Chen, H.C. Zeng, Transformation of stober silica spheres to hollow hierarchical single-crystal ZSM-5 zeolites with encapsulated metal nanocatalysts for selective catalysis, ACS Appl. Mater. Interfaces 11 (2019) 14774–14785.
[26] X. Niu, X. Li, G. Yuan, F. Feng, M. Wang, X. Zhang, Q. Wang, Hollow hierarchical silicalite-1 zeolite encapsulated PtNi bimetals for selective hydroconversion of methyl stearate into aviation fuel range alkanes, Ind. Eng. Chem. Res. 59 (18) (2020) 8601–8611.
[27] Z. Zhang, Q. Xiao, J. Gu, Effective synthesis of zeolite-encapsulated Ni nanoparticles with excellent catalytic performance for hydrogenation of CO_2 to CH_4, Dalton Trans. 49 (42) (2020) 14771–14775.
[28] B. Zhang, Y. Tian, D. Chen, L. Li, G. Li, L. Wang, X. Zhang, G. Liu, Selective steam reforming of n-dodecane over stable subnanometric NiPt clusters encapsulated in Silicalite-1 zeolite, AIChE J. 66 (2020) 1.
[29] T.M. Davis, T.O. Drews, H. Ramanan, C. He, J. Dong, H. Schnablegger, M. A. Katsoulakis, E. Kokkoli, A.V. McCormick, R.L. Penn, M. Tsapatsis, Mechanistic principles of nanoparticle evolution to zeolite crystals, Nat. Mater. 5 (5) (2006) 400–408.
[30] C. Dai, A. Zhang, L. Li, K. Hou, F. Ding, J. Li, D. Mu, C. Song, M. Liu, X. Guo, Synthesis of hollow nanocubes and macroporous monoliths of silicalite-1 by alkaline treatment, Chem. Mater. 25 (21) (2013) 4197–4205.
[31] N. Wang, Q. Sun, R. Bai, X.u. Li, G. Guo, J. Yu, In situ confinement of ultrasmall Pd clusters within nanosized silicalite-1 zeolite for highly efficient catalysis of hydrogen generation, J. Am. Chem. Soc. 138 (24) (2016) 7484–7487.
[32] Q. Sun, N. Wang, Q. Bing, R. Si, J. Liu, R. Bai, P. Zhang, M. Jia, J. Yu, Subnanometric Hybrid Pd-M(OH)2, M = Ni Co, Clusters in Zeolites as Highly Efficient Nanocatalysts for Hydrogen Generation, Chem 3 (3) (2017) 477–493.
[33] D. Duprez, M. Demicheli, P. Marecot, J. Barbier, O. Ferretti, E. Ponzi, Deactivation of steam-reforming model catalysts by coke formation: I. Kinetics of the Formation of Filamentous Carbon in the Hydrogenolysis of cyclopentane on Ni/Al_2O_3 Catalysts, J. Catal. 124 (1990) 324–335.
[34] S. Kawi, Y. Kathiraser, J. Ni, U. Oemar, Z. Li, E.T. Saw, Progress in synthesis of highly active and stable nickel-based catalysts for carbon dioxide reforming of methane, ChemSusChem 8 (21) (2015) 3556–3575.
[35] F. Wang, L. Xu, W. Shi, Syngas production from CO_2 reforming with methane over core-shell $Ni@SiO_2$ catalysts, J. CO2 Util. 16 (2016) 318–327.
[36] Y. Chen, B. Qiu, Y. Liu, Y. Zhang, An active and stable nickel-based catalyst with embedment structure for CO_2 methanation, Appl. Catal. B: Environ 269 (2020), 118801.
[37] C. Pichas, P. Pomonis, D. Petrakis, A. Ladavos, Kinetic study of the catalytic dry reforming of CH_4 with CO_2 over $La_{2-x}Sr_xNiO_4$ perovskite-type oxides, Appl. Catal., A-Gen 386 (2010) 116–123.
[38] M. Grabchenko, G. Pantaleo, F. Puleo, T.S. Kharlamova, V.I. Zaikovskii, O. Vodyankina, L.F. Liotta, Design of Ni-based catalysts supported over binary La-Ce oxides: Influence of La/Ce ratio on the catalytic performances in DRM, Catal. Today 382 (2021) 71–81.
[39] D. Ray, D. Nepak, S. Janampelli, P. Goshal, C. Subrahmanyam, Dry reforming of methane in DBD plasma over Ni-based catalysts: Influence of process conditions and support on performance and durability, Energy Technology 7 (2019) 1801008.
[40] H. Chen, Y. Shao, Y. Mu, H. Xiang, R. Zhang, Y. Chang, C. Hardacre, C. Wattanakit, Y. Jiao, X. Fan, Structured silicalite-1 encapsulated Ni catalyst supported on SiC foam for dry reforming of methane, AIChE J. 67 (2021) e17126.
[41] C. Wang, Y. Qiu, X. Zhang, Y. Zhang, N. Sun, Y. Zhao, Geometric design of a Ni@silica nano-capsule catalyst with superb methane dry reforming stability: enhanced

confinement effect over the nickel site anchoring inside a capsule shell with an appropriate inner cavity, Catal, Sci. Technol. 8 (2018) 4877–4890.
[42] F. Goodarzi, L. Kang, F.R. Wang, F. Joensen, S. Kegnaes, J. Mielby, Methanation of Carbon Dioxide over Zeolite-Encapsulated Nickel Nanoparticles, ChemCatChem 10 (2018) 1566–1570.
[43] J.-H. Kim, D.J. Suh, T.-J. Park, K.-L. Kim, Effect of metal particle size on coking during CO_2 reforming of CH_4 over Ni–alumina aerogel catalysts, Appl. Catal., A-Gen 197 (2000) 191–200.